

Bridging Microstructure and Sodium-Ion Storage Mechanism in Hard Carbon for Sodium Ion Batteries

Yuejing Zeng, Jin Yang, Huiya Yang, Yang Yang,* and Jinbao Zhao*



Cite This: *ACS Energy Lett.* 2024, 9, 1184–1191



Read Online

ACCESS |



Metrics & More

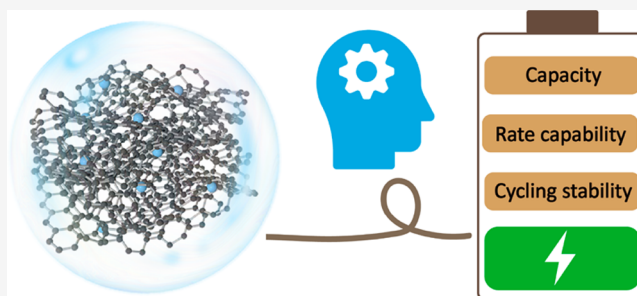


Article Recommendations



Supporting Information

ABSTRACT: Hard carbon (HC) has emerged as a strong anode candidate for sodium-ion batteries due to its high theoretical capacity and cost-effectiveness. However, its sodium storage mechanism remains contentious, and the influence of the microstructure on sodium storage performance is not yet fully understood. This study successfully correlates structural attributes with electrochemical performance, shedding light on what makes HC effective for sodium-ion storage. It is found that HC featuring larger interlayer spacing and smaller and thinner pseudographite domains is beneficial for facile Na⁺ intercalation. Conversely, the presence of a long-range ordered graphite structure should be avoided, which may result in the reduction of reversible capacity. Through detailed analysis of three commercial HC products, including in situ X-ray diffraction and Raman measurements, the “adsorption-intercalation-filling” mechanism is validated as a convincing explanation for the varying sodium storage behaviors. Consequently, this work is expected to deepen our understanding of the sodium storage mechanism and provide insightful criteria for the further development of advanced HC materials.



In recent years, the greenhouse gas emissions resulting from the extensive use of fossil fuels has presented a global challenge, and their substitution by clean energies is becoming the spotlight of worldwide research.^{1–4} This raises higher requirements for advanced battery technologies, especially for the emerging application demands of large-scale energy storage. Lithium-ion batteries (LIBs) have dominated the consumer electronics market, but the scarce abundance and rising cost of lithium resources raise urgent concerns for large-scale applications. Accordingly, the utilization of a cheaper and more abundant metal charge carrier to replace Li⁺ has attracted wide attention.^{5–7} Sodium, which occupies a similar position to lithium in the periodic table, has emerged as a promising candidate due to its widespread presence in the Earth's crust and oceans and the lower cost.^{8–11} One of the main hurdles for sodium-ion batteries (SIBs) is the development of cost-effective and high-performance electrode materials. This makes it particularly important to explore suitable anode materials for Na⁺ storage, as the commonly used graphite-anode material is not applicable.^{12–15} Hard carbon, composed of randomly oriented graphite regions and disordered turbostratic nanodomains (TNs), which provides abundant defects and nanovoids for sodium storage sites, has stood out as the most promising

anode candidate for commercial SIB implementation.^{15–21} However, the sodium storage mechanism of hard carbon (HC) remains a topic of debate due to its structural complexity. Additionally, the structure-electrochemical performance correlation has not been fully elucidated, which poses a great challenge in promoting the technological progress of hard carbon materials for SIBs.

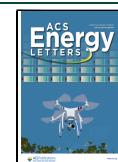
To date, researchers have employed various techniques to investigate the sodium storage characteristics of hard carbon.²² In 2000, Stevens and Dahn^{23,24} initially observed the diffraction intensity from nanopores fluctuating with voltage by in situ small-angle X-ray scattering (in situ SAXS) characterization and, thus, proposed the “intercalation-filling” mechanism to explain the sodium storage behavior of glucose-pyrolyzed hard carbon. However, this mechanism has been challenged by several experimental observations that contradict its predictions. For example, Tarascon and colleagues²⁵

Received: December 19, 2023

Revised: February 22, 2024

Accepted: February 22, 2024

Published: February 26, 2024



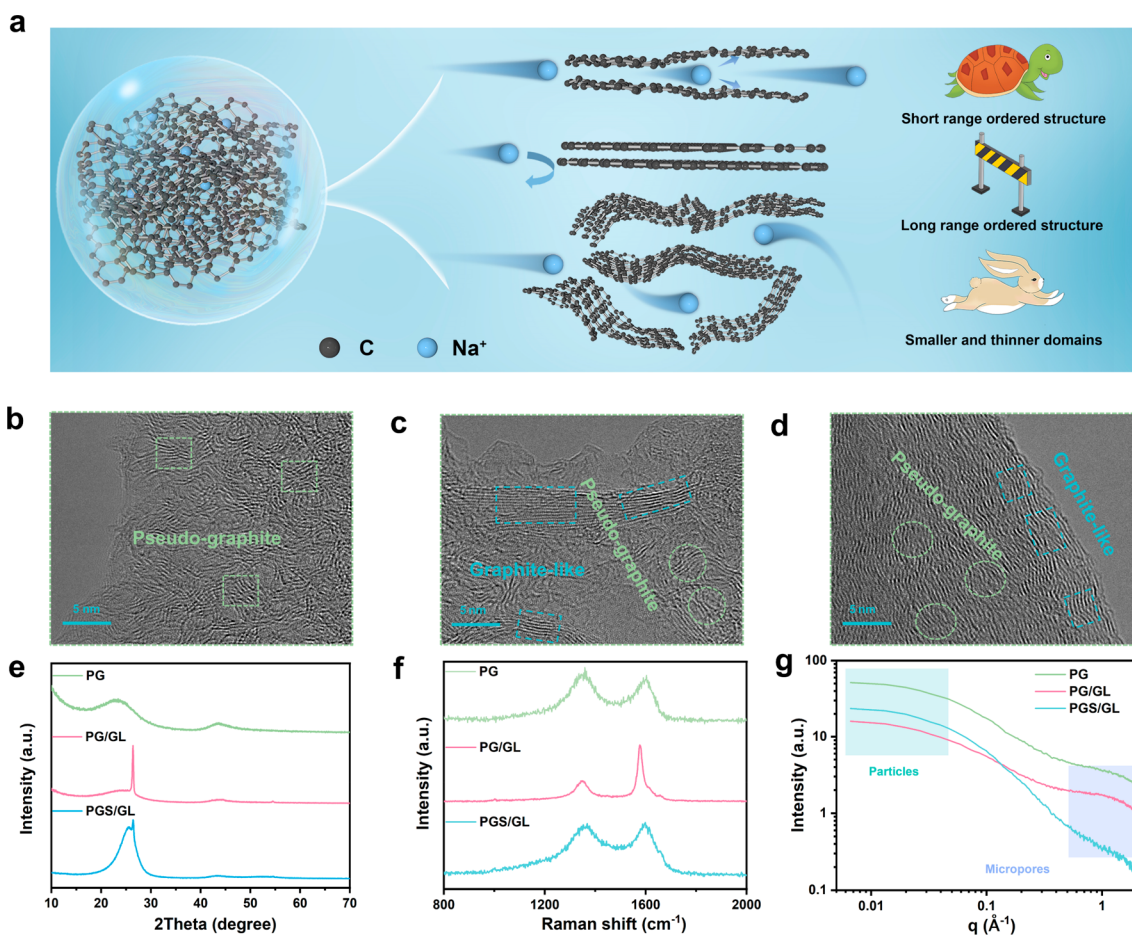


Figure 1. (a) Schematic illustration of sodium ions migrating in hard carbon with different structures. TEM diagrams of PG (b), PG/GL (c), and PGS/GL (d). (e) X-ray diffraction patterns. (f) Raman spectra. (g) SAXS profiles.

conducted in situ X-ray diffraction (XRD) measurements and did not observe the expected shift in the position of the (002) peak. They put forth the “adsorption-filling” mechanism, which suggested that the capacity contribution above 0.1 V was related to the adsorption of defects, while the plateau capacity below 0.1 V corresponds to nanopore filling. Furthermore, Ji et al.²⁶ proposed the “adsorption-intercalation-filling” mechanism. They conducted galvanostatic intermittent titration (GITT) tests and found that the apparent diffusion coefficient of Na⁺ in the slope region was larger than that in the plateau region. Despite these efforts, the sodium storage behavior of hard carbon is still ambiguous, and a clear understanding of how the basic microstructure of hard carbon relates to the mechanism of sodium storage has not been universally established.

In this study, we focused on examining the relationship between the microstructure and sodium storage mechanisms in three different types of commercial hard carbon materials with diverse structure features. They are named as hard carbon with pseudographite domains (PG), hard carbon with pseudographite and graphite-like domains (PG/GL), and hard carbon presenting pseudographite with smaller interlayer spacing and graphite-like domains (PGS/GL). Through a series of comprehensive investigations including electrochemical evaluations, in situ X-ray diffraction (XRD), and Raman measurements, how the microstructure influences sodium storage performance is uncovered. As illustrated in Figure 1a, short-range ordered quasi-graphite structures with small layer

spacing cause the carbon layer to expand during the sodium insertion process, while long-range ordered graphite domains can impede the intercalation of sodium ions. Additionally, the presence of a smaller and thinner pseudographite structure which forms the disordered turbostratic nanodomains facilitates the intercalation of sodium ions. Furthermore, the findings of this study support the validity of the “adsorption-intercalation-filling” mechanism²⁶ as an elucidation for sodium storage behaviors observed in these three distinct types of hard carbon. This work is expected to provide insightful criteria for the development of advanced hard carbon materials.

Transmission electron microscopy (TEM) visualizes that PG is mainly composed of a highly disordered and distorted pseudographite structure, showing short-range ordered lattice fringes (Figure 1b), whereas PG/GL contains both quasi-graphitic and long-range ordered graphitic-like domains (Figure 1c), and ordered graphitic domains are also demonstrated in PGS/GL (Figure 1d). Scanning electron microscopy (SEM) also exhibits the difference in the surface morphology, with spherical morphology for PG/GL (Figure S1). To further analyze the microstructure, XRD and Raman spectroscopy are performed. The XRD patterns (Figures 1e, S2) exhibit two broad diffraction peaks corresponding to the (002) and (100) peaks of amorphous carbon, except that the peaks of PG/GL and PGS/GL at about 24° show asymmetric peaks consisting of a broad peak and a sharp peak indicating the coexistence of amorphous and graphitic structures. The Bragg equation²⁷ and Debye–Scherrer equation²⁸ are utilized

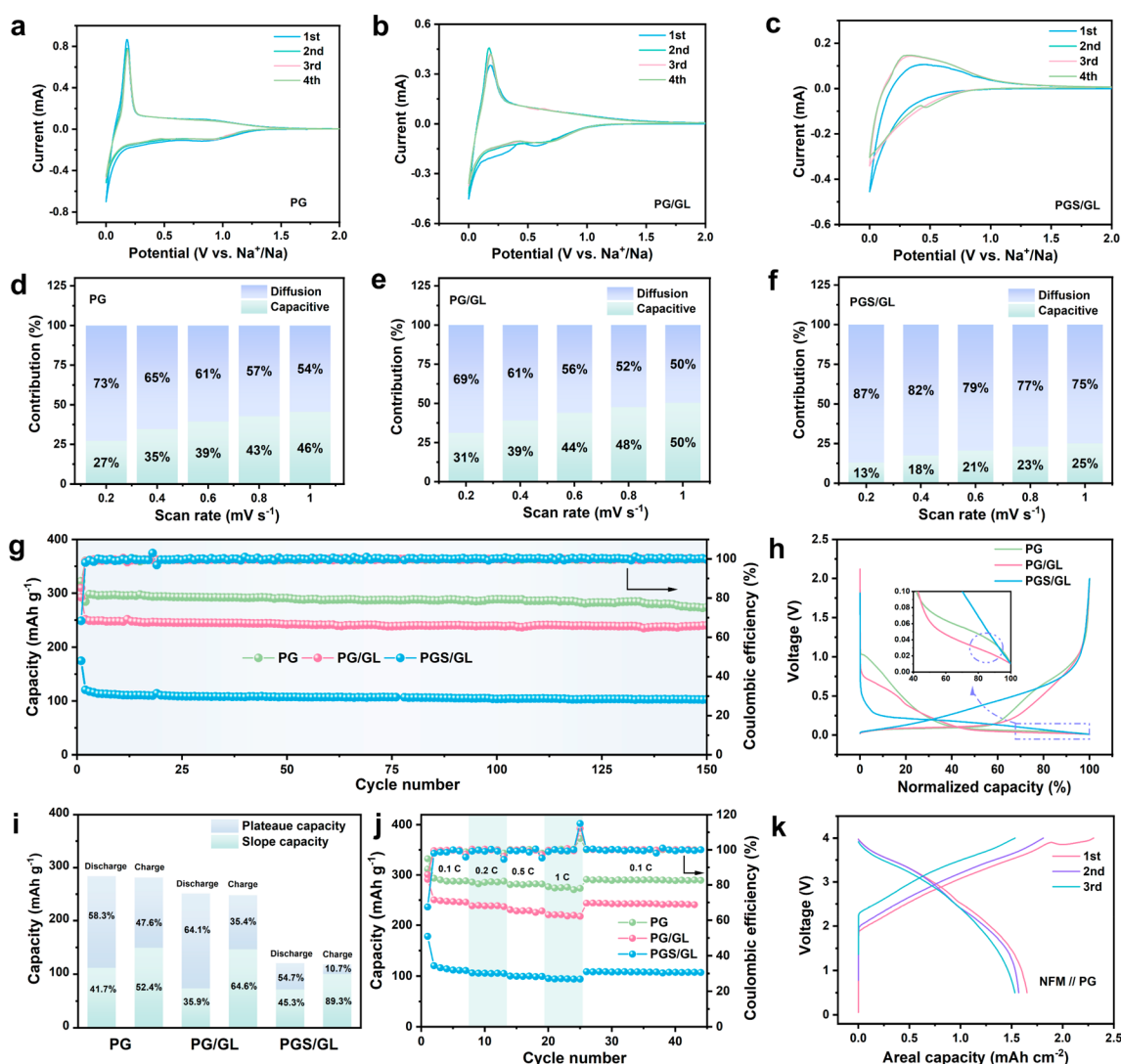


Figure 2. CV curves at scan rate of 0.1 mV s^{-1} with potential window of $2.0\text{--}0.001 \text{ V}$ for (a) PG, (b) PG/GL, and (c) PGS/GL. Percentage of diffusion-controlled and capacitive-controlled process for (d) PG, (e) PG/GL, and (f) PGS/GL. (g) Cycling performance of half-cell HC // Na at 0.1 C . (h) The initial charge–discharge curve with normalized capacity (inset: the magnified discharge curves). (i) The capacity contributed from slope and plateau region in the second cycle charge–discharge curve. (j) Rate performance. (k) The first, second, and third charge–discharge curves of full cell NFM // PG with voltage of $0.5\text{--}4.0 \text{ V}$.

to evaluate the basic structural parameters including average layer spacing (d_{002}), average layer stacking distance (L_c), the longitudinal size of structure (L_a), and the number of layers stacked in parallel (N). The empirical parameter of carbon monolayer arrangement ordering (R) proposed by Prof. J.-R. Dahn²⁹ is further introduced to measure the structural order. The structural parameters are summarized (Table S1), where PG delivers the largest layer spacing d_{002} and smaller L_a and L_c values, suggesting the existence of smaller and thinner pseudographite domains, which would be more favorable for the insertion of sodium ions. Furthermore, the smaller R value corresponds to larger electrochemical capacity.³⁰ Raman spectroscopy (Figure 1f) is further conducted to assess the microstructure with typical D and G bands of carbon material. As shown in the fitting data (Figure S3), the integral intensity ratio I_D/I_G of PG is slightly larger, proving a more disordered microstructure. The results obtained by XRD and Raman are consistent with the observation by TEM.

Furthermore, small-angle X-ray scattering (SAXS) (Figure 1g) and Brunauer–Emmett–Teller (BET) (Figure S4) are

applied to dissect the pore structure and specific surface area (S_{BET}). It is generally believed that the scattering intensity^{31,32} in $0.01\text{--}0.1 \text{ \AA}^{-1}$ is directly proportional to the specific surface area, which is consistent with the S_{BET} value. The scattering between 0.1 and 1 \AA^{-1} is originated from the micropores, whose contribution only appears in the final slope segment of Porod with Q^{-4} behavior.^{33–36} PG and PG/GL exhibit obvious shoulder girdles, indicating the existence of microporous structures. It clearly demonstrates that PG with the largest specific surface area and microporous domains indicates the most sodium storage sites.

Cyclic voltammetry (CV) is an effective means to investigate electrochemical behavior. The CV curves are achieved at a scan rate of 0.1 mV s^{-1} (Figure 2a–c), where the sharp peak near 0.1 V and the weak hump in the wide voltage range of $0.2\text{--}1.5 \text{ V}$ correspond to the plateau and the slope region in the charge–discharge profile, respectively (Figure S8). CV measurement with various scan rates of $0.2\text{--}1 \text{ mV s}^{-1}$ is carried out to further analyze the kinetic process of the sodium storage mechanism (Figures S5–S7). The law $i = av^b$ can be

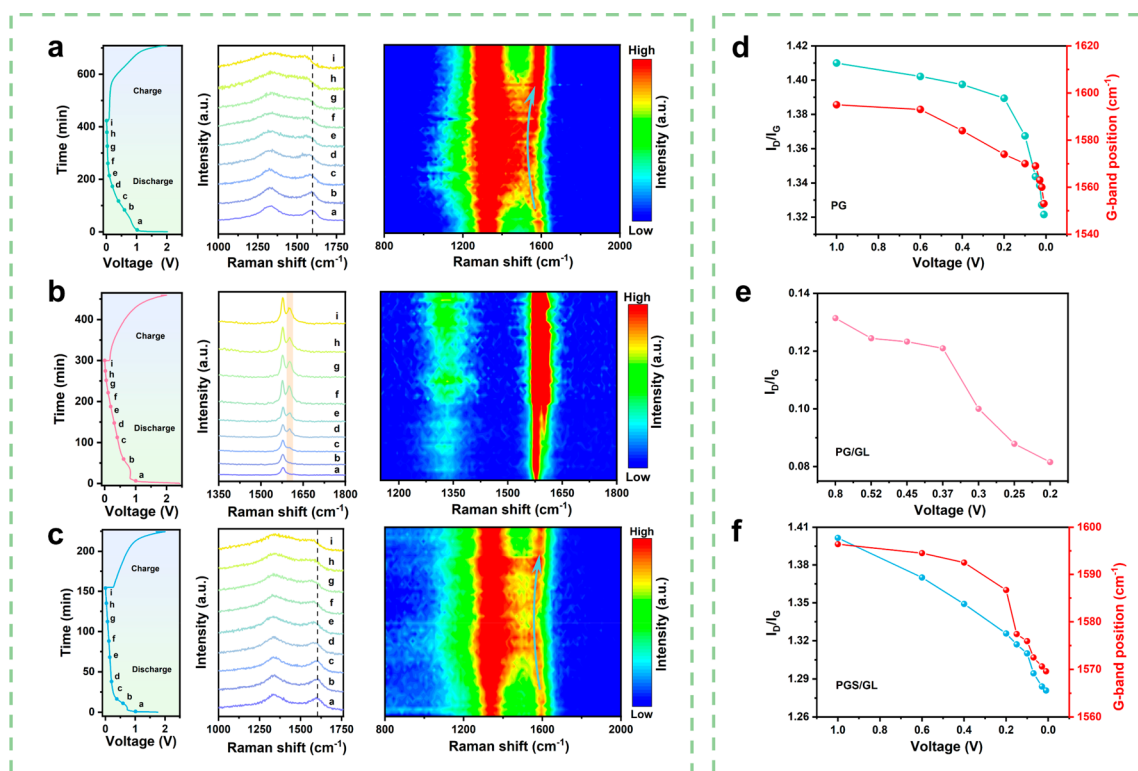


Figure 3. In situ Raman mappings in the initial discharge–charge process of (a) PG, (b) PG/GL, and (c) PGS/GL (left: the discharge–charge curve; middle: the magnified in situ Raman spectra; right: the corresponding in situ Raman contour pattern). (d) The developing of the G-band position and the I_D/I_G value as a function of voltage during discharge process for PG. (e) The I_D/I_G value varied with voltage during discharge process for PG/GL. (f) The evolution of the G-band position and the curve of I_D/I_G value variation with voltage during the discharge process for PGS/GL.

imposed to distinguish the apportion of the intercalation and capacitive reactions in the sodium storage process. In particular, $b = 1$ represents a capacitive-controlled reaction ascribed to the adsorption process, while $b = 0.5$ indicates a diffusion-controlled reaction corresponding to the intercalation process.³⁷ The b value close to 1 at the hump region (Peak P) indicates capacitive-controlled reaction in the slope region, whereas for a sharp peak (Peak Q) PG ($b = 0.65$) (Figure S5b) and PG/GL ($b = 0.71$) (Figure S6b) display a mixed-controlled process while complete diffusion-controlled for PGS/GL ($b = 0.39$) (Figure S7b). It is further verified by the standardized charge–discharge curve (Figure 2h), where PGS/GL shows diagonal change in the voltage profile, relating to the absolute diffusion-controlled process with severe concentration polarization, while PG and PG/GL exhibit voltage inflection points (enlarged curve with purple circle). Moreover, the contributions of capacitive-controlled and diffusion-controlled in the discharge process are estimated, where the proportion of the capacitive-controlled process increases with the scanning rate (Figure 2d–f), manifesting preminent rate performance. Notably, PGS/GL is dominated by diffusion-controlled at a different scanning rate, further suggesting that the sodium storage behavior is mainly based on intercalation of sodium ions.

As evidence of the above conception, a series of electrochemical characterizations are performed. The cycling performance at 0.1 C and rate performance are appraised (Figure 2g,j), where outstanding capacity retention after 100 cycles and rate performance prove prominent structure stability. It is worth mentioning that PG delivers the highest

reversible capacity of 293 mAh g^{-1} , while only 243.3 and 105.3 mAh g^{-1} are delivered for PG/GL and PGS/GL, separately. PG also presents the highest initial Coulombic efficiency (ICE) of 85.6%, compared to that of 85.2% and 65.2% for PG/GL and PGS/GL. In detail, the ratios of the slope and plateau capacity in the second charge–discharge process are demonstrated (Figure 2i), where PG delivers maximum slope capacity and total capacity resulting from the beneficial microstructure with maximal layer spacing, micropores, and defects. Especially, full cells $\text{NaNi}_{1/3}\text{Fe}_{1/3}\text{Mn}_{1/3}\text{O}_2$ (NFM) // PG are assembled with high loading (positive electrode loading of 13.5 mg cm^{-2} , N/P of 1.13) (Figure 2k), showing excellent cycling performance at 0.1 C (Figure S9), with initial discharge areal capacity of 1.67 mAh cm^{-2} .

In situ Raman spectroscopy is employed to further explore the microstructure change during the electrochemical process, as shown in Figure 3a–c. For typical carbon materials, the D band (1350 cm^{-1}) represents the A_{1g} mode of sp^2 carbon induced by respiratory vibration in disordered or defective carbon,³⁸ when the G band (1580 cm^{-1}) corresponds to the E_{2g} mode of vibration ascribed to sp^2 carbon in graphite rings or chains.³⁹ The weakening and enlargement of the C–C bond owing to the transfer of electrons or the insertion of ions in the graphite carbon layer can lead to a red-shift of the G band,^{39,40} simultaneously causing the weakening or even disappearance of the D band.^{41,42} For graphite materials, as lithiation conducted, the G band broadened and split into two peaks of $E_{2g}^{(i)}$ (1575 cm^{-1}) related to interior graphene layers of Li-GICs and $E_{2g}^{(b)}$ (1601 cm^{-1}) assigned to boundary layers.^{43–45} For PG and PGS/GL, the position of the G

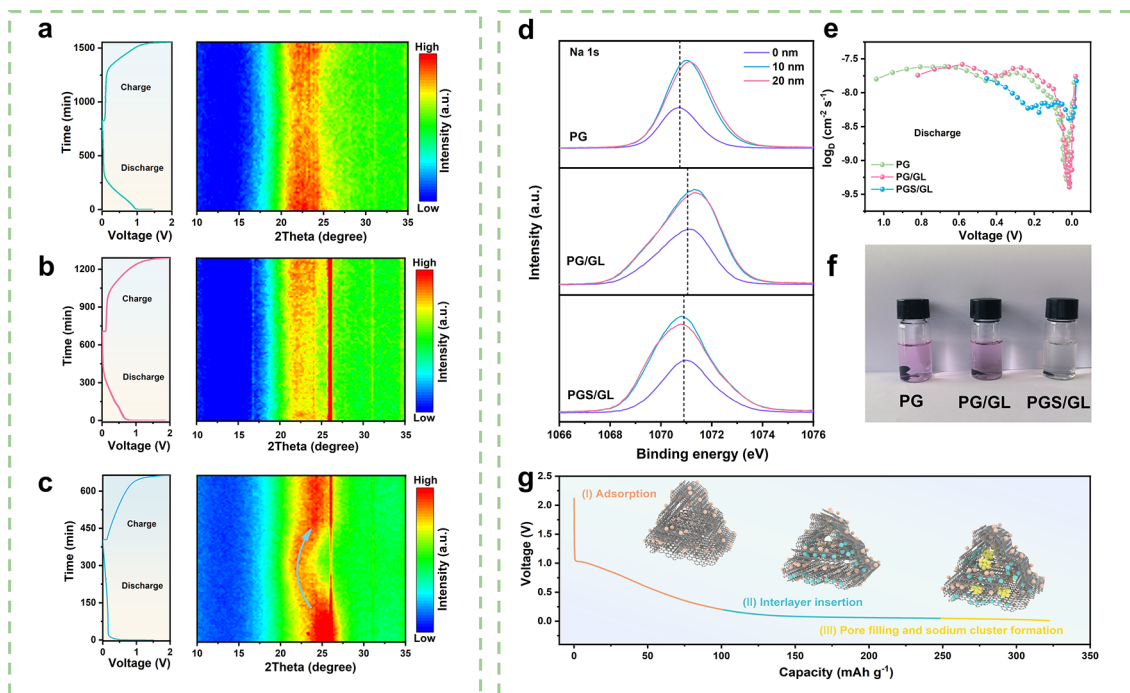


Figure 4. Operando XRD patterns during the first discharge–charge process at 0.05 C for (a) PG, (b) PG/GL, and (c) PGS/GL. (d) The depth diagrams of ex situ XPS Na 1s spectra in a fully discharged state for PG, PG/GL, and PGS/GL. (e) The Na⁺ diffusion coefficient calculated during the sodiation process. (f) The color change diagram of complete sodiation HC electrode reaction with ethanol solution with 1% phenolphthalein. (g) Schematic diagram of sodium storage in hard carbon at different stages.

band hardly shifts in the slope section during the sodiation process, while it shifts significantly in the plateau region, indicating the intercalation of sodium ions. The offset of PG (red shift 42 cm⁻¹) is larger than that of PGS/GL (red shift 26 cm⁻¹), which is accordant with the larger discharge capacity of PG. No splitting of G band is originated from the lack of adequate graphite-like domains. While for PG/GL with a broadened D band, the position of the G band hardly shifts throughout the sodiation process but gradually begins to generate a new peak at 1600 cm⁻¹, related to the boundary layers of Na-GICs. The absence of interior graphene layers of Na-GICs means no intercalation of graphite-like layers. In brief, the long-range ordered graphite-like domains hardly accommodate the intercalation of sodium ions thus lessening the capacity. Meanwhile, the variation of I_D/I_G values with voltage is also plotted in Figure 3d,e. The I_D/I_G value decreases during the sodiation process verifying the adsorption of Na⁺ in defect sites.

The distinct Raman results are attributed to the differences in the microstructure, where the XRD results can be imposed as a complement. The in situ XRD spectra during the initial sodiation and desodiation processes are displayed in Figure 4a–c, with the corresponding charge–discharge curves on the left side. As shown in Figures 4a and S10, the intensity of the (002) peak for PG diminishes in the plateau region but increases during the desodiation process, whereas the peak position hardly undergoes a significant shift throughout the process. It is noteworthy that the weakening for intensity of the (002) peak corresponds to the transformation toward disordered structure, which is caused by the insertion of sodium ions between graphite-like layers.^{24,46} The position of the (002) peak hardly moves because the original d_{002} layer spacing (0.375 nm) is large enough to accommodate sodium ions, thus causing no expansion of the layer spacing, which has

been reported in some literature.^{34,38} A similar phenomenon is observed for PG/GL (Figures 4b, S11), except that the position of the graphite peak (26.36°) also hardly shifts during the discharge process, which is in agreement with the results of in situ Raman analysis, suggesting no sodium ion insertion in graphite-like domains. In particular, for PGS/GL (Figure 4c) the (002) peak position shifts to a lower angle in the plateau section, evidencing the expansion of the interlayer spacing for pseudographitic domains, while a similar phenomenon is not observed for the graphite-like domains (26.20°), further proving the intercalation only occurs in the pseudographitic regions. Once the desodiation process occurs, the (002) peak begins to shift back, proving the contraction of the layer spacing. It can be seen that the presence of graphite-like domains does not effectively carry out the intercalation of sodium ions and therefore should be prevented in the material preparation process.

The results of in situ XRD further provide systematic understanding of the electrochemical reaction mechanism and structural evolution during the charge–discharge process. In addition, the kinetic test of the sodium storage process using GITT (Figures 4e, S12, and S14) shows that the Na⁺ diffusion coefficients for PG and PG/GL reach a minimum and then start to increase around the end of the discharge process, proving two forms of the sodium storage behaviors and the latter is more available to be pore filling inferred from literature.^{26,47,48} PGS/GL maintains the diffusion coefficient at the end of the discharge process without significant change, indicating that only sodium ion insertion occurs. In situ EIS profiles for PG (Figure S13, Figure S14b) and PG/GL (Figure S14d) also change at the end of the discharge process the same as GITT curves, which further indicates the transformation from an intercalation process of sodium ions to pore-filling behavior. XPS is conducted on hard carbon electrodes in a

fully sodiated state to analyze the state of the sodium ions stored (Figure 4d), and the peak located at 1071 eV is considered as the Na–O–C species,^{30,49} which can be found on the surface attributed to the solid electrolyte interphase layer (SEI). As demonstrated, the Na 1s peak for PG moves to a higher binding energy state with deepening of the sputtering depth from 10 to 20 nm, which proves the coexistence of sodium ions and quasi-metallic sodium.^{30,50} The same phenomenon is observed for PG/GL, whereas a similar change does not occur for PGS/GL. The existence of quasi-metallic sodium is further verified using the reaction of a hard carbon electrode in a fully sodiated state with 1% phenolphthalein in CH₃CH₂OH (Figure 4f). The color of the ethanol solution in the PG and PG/GL shows purplish-red, whereas it stays unchanged for PGS/GL. This further confirms the quasi-metallic sodium formed in the end of discharge process for both PG and PG/GL.^{30,49} Such quasi-metallic sodium mainly exists in the microporous structure of the material, which is consistent with microstructural analysis. Above all, the “adsorption-intercalation-filling” mechanism is demonstrated to be a rational elucidation for sodium storage behaviors of typical commercial hard carbon materials, as depicted in Figure 4g. Besides, another kind of commercial hard carbon (SHC) with a crystallite structure similar to that of PG is also chosen to investigate the effect of closed-pore structure on plateau capacity. SHC possesses a larger closed pore volume than that of the PG (Figure S15 and Table S2), which also delivers a larger plateau capacity.^{34,51}

In conclusion, commercial hard carbon materials with different microstructures are selected to examine the correlation between microstructure and sodium storage mechanism, which provides an understanding of the structure-electrochemical performance relationship. It is worth mentioning that hard carbon with larger d_{002} layer spacing (>0.37 nm) and smaller and thinner pseudographite domains is the key to achieve large capacity, which is beneficial for facile Na⁺ intercalation. Whereas, the presence of a long-range ordered graphite structure insufficient to accommodate the insertion of sodium ions should be avoided, which may circumvent the loss of reversible capacity. After the aforementioned microstructure requirements are met, it is also of great importance to increase the close pore volume, which will further enhance the plateau region capacity. Furthermore, through comprehensive investigation, the “adsorption-intercalation-filling” mechanism is proven to be a rational elucidation for diverse sodium storage behaviors. Above all, this study deepens the understanding of the microstructure-sodium storage mechanism relationship of hard carbon for sodium ion batteries, which provides insightful criteria for the further development of advanced hard carbon materials.

■ ASSOCIATED CONTENT

SI Supporting Information

The Supporting Information is available free of charge at <https://pubs.acs.org/doi/10.1021/acsenerylett.3c02751>.

Experimental details for the materials used in the experiment, characterizations, electrochemical measurements, the SEM, XRD, Raman, and BET patterns of the materials, the cyclic voltammograms, charge and discharge profiles, GITT and EIS profiles of the samples, additional table for the physical parameters (PDF)

■ AUTHOR INFORMATION

Corresponding Authors

Yang Yang – College of Chemistry and Chemical Engineering and State-Province Joint Engineering Laboratory of Power Source Technology for New Energy Vehicle, State Key Laboratory of Physical Chemistry of Solid Surfaces, Engineering Research Center of Electrochemical Technology, Ministry of Education, Collaborative Innovation Center of Chemistry for Energy Materials, Xiamen University, Xiamen 361005, P. R. China; Email: yangyang419@xmu.edu.cn

Jinbao Zhao – College of Chemistry and Chemical Engineering and State-Province Joint Engineering Laboratory of Power Source Technology for New Energy Vehicle, State Key Laboratory of Physical Chemistry of Solid Surfaces, Engineering Research Center of Electrochemical Technology, Ministry of Education, Collaborative Innovation Center of Chemistry for Energy Materials, Xiamen University, Xiamen 361005, P. R. China; orcid.org/0000-0002-2753-7508; Email: jbzhao@xmu.edu.cn

Authors

Yuejing Zeng – College of Chemistry and Chemical Engineering and State-Province Joint Engineering Laboratory of Power Source Technology for New Energy Vehicle, State Key Laboratory of Physical Chemistry of Solid Surfaces, Engineering Research Center of Electrochemical Technology, Ministry of Education, Collaborative Innovation Center of Chemistry for Energy Materials, Xiamen University, Xiamen 361005, P. R. China

Jin Yang – College of Chemistry and Chemical Engineering and State-Province Joint Engineering Laboratory of Power Source Technology for New Energy Vehicle, State Key Laboratory of Physical Chemistry of Solid Surfaces, Engineering Research Center of Electrochemical Technology, Ministry of Education, Collaborative Innovation Center of Chemistry for Energy Materials, Xiamen University, Xiamen 361005, P. R. China

Huiyi Yang – College of Chemistry and Chemical Engineering and State-Province Joint Engineering Laboratory of Power Source Technology for New Energy Vehicle, State Key Laboratory of Physical Chemistry of Solid Surfaces, Engineering Research Center of Electrochemical Technology, Ministry of Education, Collaborative Innovation Center of Chemistry for Energy Materials, Xiamen University, Xiamen 361005, P. R. China

Complete contact information is available at:

<https://pubs.acs.org/10.1021/acsenerylett.3c02751>

Notes

The authors declare no competing financial interest.

■ ACKNOWLEDGMENTS

This contribution is mainly supported by the National Natural Science Foundation of China (22109030 and 22021001) and the Guangdong Basic and Applied Basic Research Foundation (2019A1515111069). The authors are grateful to Tan Kah Kee Innovation Laboratory (IKKEM), Center for Micronano Fabrication and Advanced Characterization, Xiamen University for help with the XPS measurement.

REFERENCES

- (1) Shih, C. F.; Zhang, T.; Li, J. H.; Bai, C. L. Powering the Future with Liquid Sunshine. *Joule* **2018**, *2* (10), 1925–1949.
- (2) Yu, M.; Feng, X. Thin-Film Electrode-Based Supercapacitors. *Joule* **2019**, *3* (2), 338–360.
- (3) Yu, M.; Chandrasekhar, N.; Raghupathy, R. K. M.; Ly, K. H.; Zhang, H.; Dmitrieva, E.; Liang, C.; Lu, X.; Kuhne, T. D.; Mirhosseini, H.; et al. A High-Rate Two-Dimensional Polyarylimide Covalent Organic Framework Anode for Aqueous Zn-Ion Energy Storage Devices. *J. Am. Chem. Soc.* **2020**, *142* (46), 19570–19578.
- (4) Yu, M.; Shao, H.; Wang, G.; Yang, F.; Liang, C.; Rozier, P.; Wang, C. Z.; Lu, X.; Simon, P.; Feng, X. Interlayer gap widened alpha-phase molybdenum trioxide as high-rate anodes for dual-ion-intercalation energy storage devices. *Nat. Commun.* **2020**, *11* (1), 1348.
- (5) Hong, S. Y.; Kim, Y.; Park, Y.; Choi, A.; Choi, N.-S.; Lee, K. T. Charge carriers in rechargeable batteries: Na ions vs. Li ions. *Energ Environ. Sci.* **2013**, *6* (7), 2067–2081.
- (6) Yoon, G.; Kim, H.; Park, L.; Kang, K. Conditions for Reversible Na Intercalation in Graphite: Theoretical Studies on the Interplay Among Guest Ions, Solvent, and Graphite Host. *Adv. Energy Mater.* **2017**, *7* (2), No. 1601519.
- (7) Yabuuchi, N.; Kubota, K.; Dahbi, M.; Komaba, S. Research development on sodium-ion batteries. *Chem. Rev.* **2014**, *114* (23), 11636–11682.
- (8) Slater, M. D.; Kim, D.; Lee, E.; Johnson, C. S. Sodium-Ion Batteries. *Adv. Funct. Mater.* **2013**, *23* (8), 947–958.
- (9) Li, Y.; Lu, Y.; Zhao, C.; Hu, Y.-S.; Titirici, M.-M.; Li, H.; Huang, X.; Chen, L. Recent advances of electrode materials for low-cost sodium-ion batteries towards practical application for grid energy storage. *Energy Storage Mater.* **2017**, *7*, 130–151.
- (10) Slater, M. D.; Kim, D.; Lee, E.; Johnson, C. S. Correction: Sodium-Ion Batteries. *Adv. Funct. Mater.* **2013**, *23* (26), 3255–3255.
- (11) Kim, H.; Kim, H.; Ding, Z.; Lee, M. H.; Lim, K.; Yoon, G.; Kang, K. Recent Progress in Electrode Materials for Sodium-Ion Batteries. *Adv. Energy Mater.* **2016**, *6* (19), No. 1600943.
- (12) Wang, Q.; Zhao, C.; Lu, Y.; Li, Y.; Zheng, Y.; Qi, Y.; Rong, X.; Jiang, L.; Qi, X.; Shao, Y.; et al. Advanced Nanostructured Anode Materials for Sodium-Ion Batteries. *Small* **2017**, *13* (42), No. 1701835.
- (13) Xie, F.; Xu, Z.; Guo, Z.; Titirici, M.-M. Hard carbons for sodium-ion batteries and beyond. *Prog. Energy* **2020**, *2* (4), No. 042002.
- (14) Liu, X.; Wang, T.; Zhang, T.; Sun, Z.; Ji, T.; Tian, J.; Wang, H.; Hao, X.; Liu, H.; Chao, D. Solvated Sodium Storage via a Coadsorbative Mechanism in Microcrystalline Graphite Fiber. *Adv. Energy Mater.* **2022**, *12* (45), No. 2202388.
- (15) Wang, G.; Yu, M.; Feng, X. Carbon materials for ion-intercalation involved rechargeable battery technologies. *Chem. Soc. Rev.* **2021**, *50* (4), 2388–2443.
- (16) Franklin, R. E. Crystallite growth in graphitizing and non-graphitizing carbons. *Proc. R. Soc. London A* **1951**, *209* (1097), 196–218.
- (17) Qi, Y.; Lu, Y.; Ding, F.; Zhang, Q.; Li, H.; Huang, X.; Chen, L.; Hu, Y. S. Slope-Dominated Carbon Anode with High Specific Capacity and Superior Rate Capability for High Safety Na-Ion Batteries. *Angew. Chem.* **2019**, *131* (13), 4405–4409.
- (18) Lu, Y.; Zhao, C.; Qi, X.; Qi, Y.; Li, H.; Huang, X.; Chen, L.; Hu, Y.-S. Pre-Oxidation-Tuned Microstructures of Carbon Anodes Derived from Pitch for Enhancing Na Storage Performance. *Adv. Energy Mater.* **2018**, *8* (27), No. 1800108.
- (19) Qi, Y.; Lu, Y.; Liu, L.; Qi, X.; Ding, F.; Li, H.; Huang, X.; Chen, L.; Hu, Y.-S. Retarding graphitization of soft carbon precursor: From fusion-state to solid-state carbonization. *Energy Storage Mater.* **2020**, *26*, 577–584.
- (20) Chen, X. Y.; Tian, J. Y.; Li, P.; Fang, Y. L.; Fang, Y. J.; Liang, X. M.; Feng, J. W.; Dong, J.; Ai, X. P.; Yang, H. X.; et al. An Overall Understanding of Sodium Storage Behaviors in Hard Carbons by an “Adsorption-Intercalation/Filling” Hybrid Mechanism. *Adv. Energy Mater.* **2022**, *12* (24), No. 2200886.
- (21) Li, T.; Liu, Z.; Gu, Y.; Tang, Y.; Huang, F. Hierarchically porous hard carbon with graphite nanocrystals for high-rate sodium ion batteries with improved initial Coulombic efficiency. *J. Alloys Compd.* **2020**, *817*, No. 152703.
- (22) Sun, N.; Guan, Z.; Liu, Y.; Cao, Y.; Zhu, Q.; Liu, H.; Wang, Z.; Zhang, P.; Xu, B. Extended “Adsorption–Insertion” Model: A New Insight into the Sodium Storage Mechanism of Hard Carbons. *Adv. Energy Mater.* **2019**, *9* (32), No. 1901351.
- (23) Stevens, D. A.; Dahn, J. R. High Capacity Anode Materials for Rechargeable Sodium-Ion Batteries. *J. Electrochem. Soc.* **2000**, *147* (4), 1271–1273.
- (24) Stevens, D. A.; Dahn, J. R. The Mechanisms of Lithium and Sodium Insertion in Carbon Materials. *J. Electrochem. Soc.* **2001**, *148* (8), A803–A811.
- (25) Zhang, B.; Ghimbeu, C. M.; Laberty, C.; Vix-Guterl, C.; Tarascon, J.-M. Correlation Between Microstructure and Na Storage Behavior in Hard Carbon. *Adv. Energy Mater.* **2016**, *6* (1), No. 1501588.
- (26) Bommier, C.; Surta, T. W.; Dolgos, M.; Ji, X. New Mechanistic Insights on Na-Ion Storage in Nongraphitizable Carbon. *Nano Lett.* **2015**, *15* (9), 5888–5892.
- (27) Bragg, W. H.; Bragg, W. L. The reflection of X-rays by crystals. *Proc. R. Soc. London A* **1913**, *88* (605), 428–438.
- (28) Scherrer, P. Estimation of the size and internal structure of colloidal particles by means of Röntgen. *Nachr. Ges. Wiss. Göttingen* **1918**, *2*, 96–100.
- (29) Zheng, T.; Xing, W.; Dahn, J. R. Carbons prepared from coals for anodes of lithium-ion cells. *Carbon* **1996**, *34* (96), 1501–1507.
- (30) Wang, Z.; Feng, X.; Bai, Y.; Yang, H.; Dong, R.; Wang, X.; Xu, H.; Wang, Q.; Li, H.; Gao, H.; et al. Probing the Energy Storage Mechanism of Quasi-Metallic Na in Hard Carbon for Sodium-Ion Batteries. *Adv. Energy Mater.* **2021**, *11* (11), No. 2003854.
- (31) Navarro-Suárez, A. M.; Saurel, D.; Sánchez-Fontecoba, P.; Castillo-Martínez, E.; Carretero-González, J.; Rojo, T. Temperature effect on the synthesis of lignin-derived carbons for electrochemical energy storage applications. *J. Power Sources* **2018**, *397*, 296–306.
- (32) Simone, V.; Boulineau, A.; de Geyer, A.; Rouchon, D.; Simonin, L.; Martinet, S. Hard carbon derived from cellulose as anode for sodium ion batteries: Dependence of electrochemical properties on structure. *J. Energy Chem.* **2016**, *25* (5), 761–768.
- (33) Chen, Y.; Li, F.; Guo, Z.; Song, Z.; Lin, Y.; Lin, W.; Zheng, L.; Huang, Z.; Hong, Z.; Titirici, M.-M. Sustainable and scalable fabrication of high-performance hard carbon anode for Na-ion battery. *J. Power Sources* **2023**, *557*, No. 232534.
- (34) Li, Y.; Lu, Y.; Meng, Q.; Jensen, A. C. S.; Zhang, Q.; Zhang, Q.; Tong, Y.; Qi, Y.; Gu, L.; Titirici, M. M.; et al. Regulating Pore Structure of Hierarchical Porous Waste Cork-Derived Hard Carbon Anode for Enhanced Na Storage Performance. *Adv. Energy Mater.* **2019**, *9* (48), No. 1902852.
- (35) Li, Q.; Liu, X.; Tao, Y.; Huang, J.; Zhang, J.; Yang, C.; Zhang, Y.; Zhang, S.; Jia, Y.; Lin, Q.; et al. Sieving carbons promise practical anodes with extensible low-potential plateaus for sodium batteries. *National Science Review* **2022**, *9* (8), No. nwac084.
- (36) Chu, Y.; Zhang, J.; Zhang, Y.; Li, Q.; Jia, Y.; Dong, X.; Xiao, J.; Tao, Y.; Yang, Q. H. Reconfiguring Hard Carbons with Emerging Sodium-Ion Batteries: A Perspective. *Adv. Mater.* **2023**, *35* (31), No. 2212186.
- (37) Zhao, Y.; Ye, J.; Zhang, P.; Li, Z.; Zhao, H. Abnormal preferential oxygen functionalization on the surface of soft/hard carbon for sodium storage. *Appl. Surf. Sci.* **2022**, *602*, No. 154336.
- (38) Qiu, S.; Xiao, L. F.; Sushko, M. L.; Han, K. S.; Shao, Y. Y.; Yan, M. Y.; Liang, X. M.; Mai, L. Q.; Feng, J. W.; Cao, Y. L.; et al. Manipulating Adsorption-Insertion Mechanisms in Nanostructured Carbon Materials for High-Efficiency Sodium Ion Storage. *Adv. Energy Mater.* **2017**, *7* (17), No. 1700403.
- (39) Hardwick, L. J.; Ruch, P. W.; Hahn, M.; Scheifele, W.; Kötz, R.; Novák, P. In situ Raman spectroscopy of insertion electrodes for

lithium-ion batteries and supercapacitors: First cycle effects. *J. Phys. Chem. Solids* **2008**, *69* (5–6), 1232–1237.

(40) Komaba, S.; Murata, W.; Ishikawa, T.; Yabuuchi, N.; Ozeki, T.; Nakayama, T.; Ogata, A.; Gotoh, K.; Fujiwara, K. Electrochemical Na Insertion and Solid Electrolyte Interphase for Hard-Carbon Electrodes and Application to Na-Ion Batteries. *Adv. Funct. Mater.* **2011**, *21* (20), 3859–3867.

(41) Zhong, X.; Li, Y.; Zhang, L.; Tang, J.; Li, X.; Liu, C.; Shao, M.; Lu, Z.; Pan, H.; Xu, B. High-Performance Sodium-Ion Batteries Based on Nitrogen-Doped Mesoporous Carbon Spheres with Ultrathin Nanosheets. *ACS Appl. Mater. Interfaces* **2019**, *11* (3), 2970–2977.

(42) Huang, S.; Li, Z.; Wang, B.; Zhang, J.; Peng, Z.; Qi, R.; Wang, J.; Zhao, Y. N-Doping and Defective Nanographitic Domain Coupled Hard Carbon Nanoshells for High Performance Lithium/Sodium Storage. *Adv. Funct. Mater.* **2018**, *28* (10), No. 1706294.

(43) Yadegari, H.; Koronfel, M. A.; Wang, K.; Thornton, D. B.; Stephens, I. E. L.; Molteni, C.; Haynes, P. D.; Ryan, M. P. Operando Measurement of Layer Breathing Modes in Lithiated Graphite. *ACS Energy Letters* **2021**, *6* (4), 1633–1638.

(44) Sole, C.; Drewett, N. E.; Hardwick, L. J. In situ Raman study of lithium-ion intercalation into microcrystalline graphite. *Faraday Discuss.* **2014**, *172* (0), 223–237.

(45) Zhu, Z.; Cheng, F.; Hu, Z.; Niu, Z.; Chen, J. Highly stable and ultrafast electrode reaction of graphite for sodium ion batteries. *J. Power Sources* **2015**, *293*, 626–634.

(46) He, X. X.; Lai, W. H.; Liang, Y.; Zhao, J. H.; Yang, Z.; Peng, J.; Liu, X. H.; Wang, Y. X.; Qiao, Y.; Li, L.; et al. Achieving All Plateau and High Capacity Sodium Insertion in Topological Graphitized Carbon. *Adv. Mater.* **2023**, *35* (40), No. 2302613.

(47) Zhao, J.; He, X. X.; Lai, W. H.; Yang, Z.; Liu, X. H.; Li, L.; Qiao, Y.; Xiao, Y.; Li, L.; Wu, X.; et al. Catalytic Defect-Repairing Using Manganese Ions for Hard Carbon Anode with High-Capacity and High-Initial-Coulombic-Efficiency in Sodium-Ion Batteries. *Adv. Energy Mater.* **2023**, *13* (18), No. 2300444.

(48) Li, Y.; Hu, Y.-S.; Titirici, M.-M.; Chen, L.; Huang, X. Hard Carbon Microtubes Made from Renewable Cotton as High-Performance Anode Material for Sodium-Ion Batteries. *Adv. Energy Mater.* **2016**, *6* (18), No. 1600659.

(49) Zhu, Z.; Zhong, W.; Zhang, Y.; Dong, P.; Sun, S.; Zhang, Y.; Li, X. Elucidating electrochemical intercalation mechanisms of biomass-derived hard carbon in sodium-/potassium-ion batteries. *Carbon Energy* **2021**, *3* (4), 541–553.

(50) Yu, Z. E.; Lyu, Y.; Wang, Y.; Xu, S.; Cheng, H.; Mu, X.; Chu, J.; Chen, R.; Liu, Y.; Guo, B. Hard carbon micro-nano tubes derived from kapok fiber as anode materials for sodium-ion batteries and the sodium-ion storage mechanism. *Chem. Commun.* **2020**, *56* (5), 778–781.

(51) Tang, Z.; Zhang, R.; Wang, H.; Zhou, S.; Pan, Z.; Huang, Y.; Sun, D.; Tang, Y.; Ji, X.; Amine, K.; et al. Revealing the closed pore formation of waste wood-derived hard carbon for advanced sodium-ion battery. *Nat. Commun.* **2023**, *14* (1), 6024.